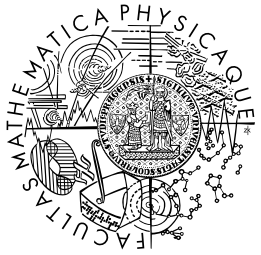

FACULTY
OF MATHEMATICS
AND PHYSICS
Charles University

SUMMARY OF DOCTORAL THESIS

Miroslav Halló

Influence of velocity model uncertainty in earthquake source inversions

Department of Geophysics

Supervisor of the doctoral thesis:	doc. RNDr. František Gallovič, Ph.D.
Study programme:	Physics
Study branch:	Geophysics

Prague 2018

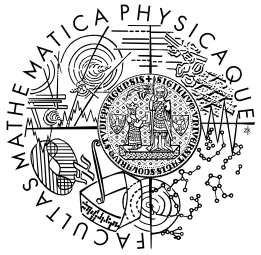

MATEMATICKO-FYZIKÁLNÍ FAKULTA
Univerzita Karlova

AUTOREFERÁT DIZERTAČNÍ PRÁCE

Miroslav Halló

Vliv neurčitosti rychlostního modelu při studiu zemětřesného zdroje

Katedra geofyziky

Vedoucí dizertační práce:	doc. RNDr. František Gallovič, Ph.D.
Studijní program:	Fyzika
Studijní obor:	Geofyzika

Praha 2018

Dizertace byla vypracována na základě výsledků získaných v letech 2014-2018 během doktorandského studia na Katedře geofyziky MFF UK a stáže na Disaster Prevention Research Institute, Kyoto University, Japan.

Dizertant:
RNDr. Miroslav Halló
Katedra geofyziky MFF UK
V Holešovičkách 2, 180 00 Praha 8

Školitel:
doc. RNDr. František Gallovič, Ph.D.
Katedra geofyziky MFF UK
V Holešovičkách 2, 180 00 Praha 8

Oponenti:
Dr. Zacharie Duputel
Institut de Physique du Globe de Strasbourg
Ecole et Observatoire des Sciences de la Terre
5 rue René Descartes, F-67084 Strasbourg cedex, France

RNDr. Václav Vavryčuk, DrSc.
Geofyzikální ústav Akademie věd, v. v. i.
Boční II/1401, 141 31 Praha 4

Předsedkyně oborové rady:
doc. RNDr. Hana Čížková, Ph.D.
Katedra geofyziky MFF UK
V Holešovičkách 2, 180 00 Praha 8

Obhajoba dizertace se koná dne 21. 9. 2018 v 14:00 hodin před komisí pro obhajoby dizertačních prací v oboru Geofyzika v budově MFF UK, Ke Karlovu 3, Praha 2 v místnosti M252.

S dizertací je možno se seznámit v PGS MFF UK, Ke Karlovu 3, Praha 2.

Contents

Introduction

Earthquake ground motions originate from rupture processes on faults in Earth. Constraints on earthquake source models are important for better understanding of earthquake physics and for seismic hazard analysis, which is particularly significant for construction engineering and disaster mitigation planning. In addition, earthquake source models serve as input for studies like analysis of the earthquake energy budget (e.g., Kanamori & Rivera 2006), dynamic stress drop analysis, Coulomb stress modeling, etc. Realistic estimate of the uncertainty of earthquake source models is essential for evaluation of solution quality. Strictly speaking, any interpretation of centroid moment tensor or finite-extent model requires proper assessment of their uncertainty (e.g., Sokos et al. 2015; Dettmer et al. 2014; Duputel et al. 2015).

Earthquake source models are inferred from observed waveforms by inverse modeling, which is subject to uncertainty. Synthetic waveforms required by the inverse modeling are computed using Green's functions (GFs) representing response of Earth's crust to an impulse stimulus. In the case of large tectonic earthquakes, the major source of uncertainty of the inferred source models is related to the uncertainty of the GFs due to the inaccuracy of the crustal models considered. In practical applications, the uncertainties of the inferred source parameters are typically estimated by accepting all models within a given threshold on the misfit value (e.g., Piatanesi et al. 2007; Valentine & Trampert 2012; Zahradník & Custódio 2012; Gallovič & Zahradník 2012). However, the value of such threshold is not based on a proper analysis of the underlying origin of the uncertainty. We point out that imprecise knowledge of the velocity model can lead to spurious non-double-couple components in moment tensor inversions (Zahradník et al. 2015) and artificial slip-rate peaks in slip inversions (Gallovič et al. 2015).

Earthquake source model inversions with the assessment of the solution uncertainty are usually performed in the Bayesian probabilistic framework (e.g., Yagi & Fukahata 2011; Minson et al. 2013, 2014; Dettmer et al. 2007, 2014; Duputel et al. 2014, 2015; Kubo et al. 2016a; Mustać & Tkalčić 2016; Vackář et al. 2017). In this way a prior information on the physical model is specified, which is then updated to a conditional posterior probability on model parameters affected by the observed data (e.g., Tarantola & Valette 1982; Tarantola 2005). In such framework, the assumptions on uncertainty of the observed waveforms and computed GFs can be incorporated, e.g., by means of Gaussian covariance matrices. The inferred solution is then represented by the conditional posterior probability on model parameters. The uncertainty of the inferred source model may be then assessed by analytical formulas (if possible) or by ensemble of solutions drawn from the posterior probability density.

The covariance matrix of GFs has been considered by other researchers, however a proper analysis of the GFs' uncertainty has not been done yet. In particular, Yagi & Fukahata (2011) and Minson et al. (2013) considered diagonal GF covariance matrix in their Bayesian slip inversion, treating the GF variance as an unknown parameter. Duputel et al. (2012) showed the importance of considering the full covariance matrix of GF in the moment tensor inversion. However,

in their examples they assume that the major origin of the error is due to the centroid mislocation. That study was extended by Duputel et al. (2014, 2015), who proposed to estimate the full covariance matrix approximately by considering linear relationship between the GFs and random, generally 3D, perturbations of the velocity model. However, their approach requires evaluation of sensitivity kernels, which are, in practice, expensive to acquire. An alternative approach is represented by "empirical" estimation of the covariances from data residuals in so-called hierarchical inversions (Dettmer et al. 2007, 2014; Mustać & Tkalčić 2016). In particular, Dettmer et al. (2007, 2014) took into account the non-stationary character of the noise by scaling rows and columns of the covariance matrix by running averages of the residual waveforms.

This research is focused on the influence of uncertainty of a crustal velocity model by means of uncertainty of GFs in earthquake source inversions. We first perform Monte-Carlo simulations of GFs in randomly perturbed velocity models to reveal the effects of the imprecise velocity model on the synthetic waveforms. We derive closed-form formulas for approximate covariance functions to obtain fast and effective characterization of the GFs' uncertainty avoiding any demanding computations (Hallo & Gallovič 2016). The proposed approximate covariance functions are tested on Bayesian moment tensor inversions of synthetic data, and bench-marked on real earthquake from Corinth Gulf, Greece. In particular, experiments with the large number of synthetic target datasets obtained by randomly perturbing velocity models reveal the effects of the imprecise velocity model on the inferred moment tensors. Inversion tests with the approximate covariance functions of GFs show that the posterior covariance matrix of model parameters provides accordant realistic estimate of the moment tensor uncertainties.

In the consecutive research, Hallo et al. (2017), we incorporated the approximate covariances into the Bayesian full-waveform centroid moment tensor inversion code package ISOLA-ObsPy (Vackář et al. 2017). The modification of the ISOLA-ObsPy with assessment of GF uncertainties was applied on foreshocks and aftershocks of the 2016 Kumamoto, Kyushu, Japan, earthquake sequence. The assessment of the uncertainties of the centroid moment tensors showed to be beneficial in terms of interpretation of the results in the seismo-tectonic framework.

Further, we developed a new Bayesian parametric fault slip inversion, which accounts for the GFs' uncertainty again by means of the approximate covariance functions. Our non-linear finite-extent source inversion method relies on self-adapting parametrization of slip function by means of varying number of spline control points on the fault surface. The posterior probability density is then sampled by trans-dimensional Markov chain Monte Carlo algorithm. Performance of the slip inversion method is demonstrated on the destructive M_w7.1 mainshock of the 2016 Kumamoto sequence. We infer ensemble of more than 590k possible finite source models following the posterior probability density. This allows us to inspect which features of the source model are reliable and which are rather artifacts caused by imprecise knowledge of a crustal velocity model.

1. Approximation of Green's functions uncertainty

In the Bayesian framework the uncertainty of source inversions relies on statistical description of the GF uncertainty. In accordance with other authors, we assume that it can be described by a correlated multivariate Gaussian probability density function (PDF) characterized by a covariance matrix. To understand the relation between the uncertainty of the GFs and imprecise knowledge of the velocity model, we analyze the dependence of the covariance on velocity model perturbations using Monte-Carlo (MC) simulations considering stations at various distances and data in various frequency ranges. Then we propose methodologies for approximate yet simple estimation of the GF covariances.

1.1 Monte-Carlo estimation

We treat a GF due to randomly perturbed velocity model as a random function $x(t)$. The cross-covariance function (XCF) of two random GFs $x(t)$ and $y(t)$ is defined as

$$xcov(t,\tau) \stackrel{def}{=} E\Big\{ \Big[x(t) - E\{x(t)\}\Big] \Big[y(t+\tau) - E\{y(t+\tau)\}\Big] \Big\} = \tag{1.1}$$

$$= E\Big\{x(t)y(t+\tau)\Big\} - E\Big\{x(t)\Big\}\, E\Big\{y(t+\tau)\Big\}, \tag{1.2}$$

where $E\{\cdot\}$ denotes expectation (mean over realizations of $x(t)$ and $y(t)$), t is time and τ is a time lag between samples (e.g., Marple 1986). Auto-covariance function (CF) can be derived from (1.2) considering $y(t) = x(t)$,

$$cov(t,\tau) = E\Big\{x(t)x(t+\tau)\Big\} - E\Big\{x(t)\Big\}\, E\Big\{x(t+\tau)\Big\}. \tag{1.3}$$

A straightforward, though computationally demanding, approach to evaluate the covariances is by MC simulations (e.g., Tarantola 2005, pp. 41–55), where the expectations in (1.2) and (1.3) are directly obtained from a set of possible GFs for a particular source-receiver settings. For this purpose we consider an initial 1D layered velocity model and its 1500 random variations (Fig. 1.1a). In particular, following Tarantola (2005, pp. 164–170), we randomly vary logarithms of incompressibility modulus κ^*, shear modulus μ^*, and layer thicknesses. The parameters are changed independently to each other and also independently in all layers, assuming Gaussian distribution characterized by standard deviation σ_M expressed in percentage of the initial (mean) value.

We simulate GFs for source-receiver distances $10, 50, 100\,km$ in the random realizations of the velocity models by discrete wavenumber method (Bouchon 1981), assuming a Dirac delta function as the source time function. GFs computed in the mean velocity model are referred to as the "mother" GFs. Fig. 1.1b shows example of the generated GFs for one source-receiver distance. They are similar in shape even though the velocity model perturbations are as large as 10 % in the present example (maximal correlation coefficients are higher than 0.7 for all the generated GFs). A pronounced effect of the velocity model variations is represented by shifts of the generated waveforms in time. These time

shifts (evaluated in this synthetic test from waveform cross-correlation lag from low-frequency waveforms to avoid cycle skipping) have approximately Gaussian distribution with standard deviation σ_t as demonstrated by the histogram in Fig. 1.1c. As illustrated in Fig. 1.1d, the characteristic width L of the time shift distribution defined as $L = 4\sigma_t$ increases approximately linearly with the velocity model perturbations σ_M with rate depending on the epicentral distance.

The CFs determined by Eq. (1.3) from a set of possible GFs for a particular source-receiver settings could be used, in principle, for construction of the full covariance matrix (example shown in Fig. 1.2a). However, the MC technique is very demanding on computational power as there is required an enormous set of possible GFs.

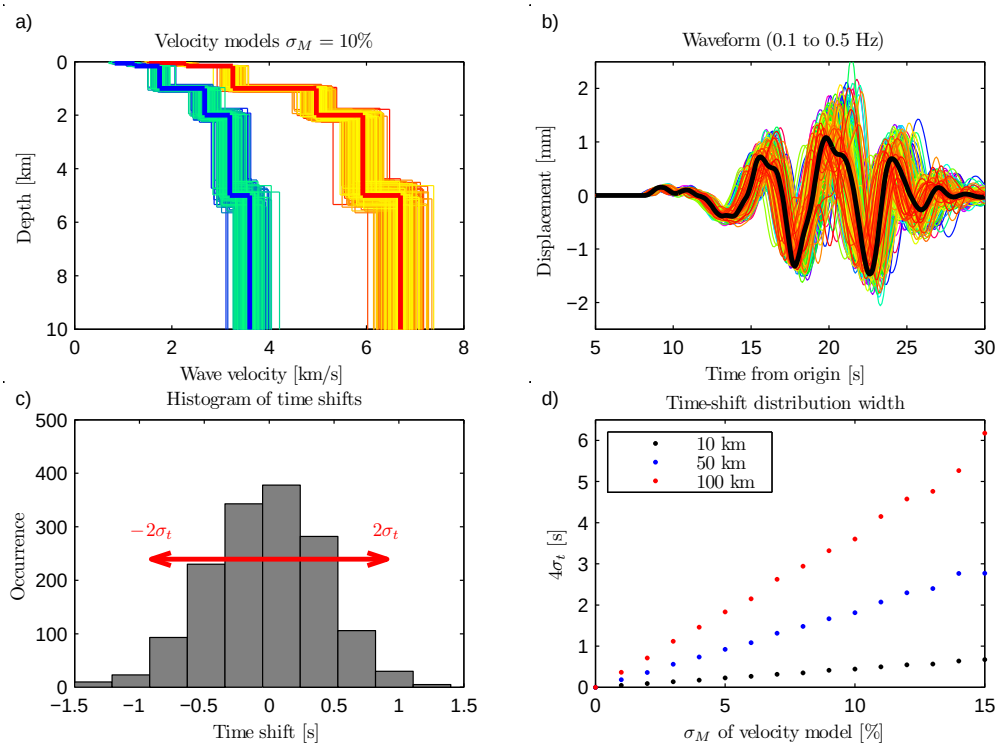

Figure 1.1: *Monte-Carlo simulations.* ***a)*** *Example of the set of randomly perturbed velocity models with standard deviation $\sigma_M = 10\,\%$. The red/blue lines are the mean P-/S-wave velocity profiles and warm/cold colors are the P-/S-wave velocities of the perturbed models, respectively.* ***b)*** *Examples of the GFs at one component simulated by the discrete wavenumber method for the source-receiver distance of 50 km ($\sigma_M = 10\,\%$). The black line is the "mother" GF calculated in the mean velocity model. Other colors of waveforms have no meaning and are used only for clearer view.* ***c)*** *Distribution of time shifts of GFs from panel* ***b*** *estimated from waveforms filtered at very low frequencies ($0.05 - 0.09\,Hz$) to avoid cycle skipping. The red line shows its characteristic width $4\sigma_t$.* ***d)*** *The dependence of the characteristic width of the time shift distribution ($4\sigma_t$) on the strength of the velocity model perturbations σ_M for three source-receiver distances.*

1.2 Approximate covariance functions

Here we propose to substitute the demanding MC estimation of the GF covariance by a simplified approach, assuming that the only effect of the velocity model

perturbations on the covariances is the time shift of the mother GFs. As we demonstrate later, despite of this assumption, the approximate covariances (example shown in Fig. 1.2c) reproduce variations of both the arrival time and the waveform amplitudes.

Let us derive the approximate formulas for XCF of two, generally different, waveforms with random time shifts. We consider two "mother" waveforms $f(t)$ and $g(t)$ representing GFs in the mean velocity model. Assuming that these waveforms are randomly shifted in time, we define new (random) waveforms $x(t) = f(t - l_1)$ and $y(t) = g(t - l_1 - l_{12})$. The time shift l_1 is random but the same for both signals, while l_{12} characterizes their relative random time shift. We denote PDFs of l_1 and l_{12} as $p_1(l_1)$ and $p_{12}(l_{12})$, respectively. Expectations $E\{\cdot\}$ in Eq. (1.2) can be evaluated using "mother" waveforms and the PDFs $p_1(l_1)$ and $p_{12}(l_{12})$ as

$$E\Big\{x(t)\Big\} = \int_{-\infty}^{\infty} f(t - l_1)\, p_1(l_1)\, \mathrm{d}l_1 \tag{1.4}$$

$$E\Big\{y(t+\tau)\Big\} = \int_{-\infty}^{\infty}\int_{-\infty}^{\infty} g(t + \tau - l_1 - l_{12})\, p_{12}(l_{12})\, p_1(l_1)\, \mathrm{d}l_{12}\, \mathrm{d}l_1 \tag{1.5}$$

$$E\Big\{x(t)y(t+\tau)\Big\} = \int_{-\infty}^{\infty}\int_{-\infty}^{\infty} f(t - l_1)\, g(t + \tau - l_1 - l_{12})\, p_{12}(l_{12})\, p_1(l_1)\, \mathrm{d}l_{12}\, \mathrm{d}l_1 \tag{1.6}$$

The XCF formula for general PDFs $p_1(l_1)$ and $p_{12}(l_{12})$ can be obtained by putting (1.4), (1.5) and (1.6) into Eq. (1.2) requiring only specification of the "mother" waveforms and PDFs of the time shifts. It is, in principle, applicable in covariance matrix estimation in this form; nevertheless, the formula can be further simplified by assuming that the time-shift l_1 is uniformly distributed in the time interval from $(-L_1)/2$ to $(+L_1)/2$ and the time-shift l_{12} is uniformly distributed from $(-L_{12})/2$ to $(+L_{12})/2$. The expectations of the random processes in (1.4), (1.5) and (1.6) then simplify to

$$E\Big\{x(t)\Big\} = \frac{1}{L_1}\int_{-\frac{L_1}{2}}^{\frac{L_1}{2}} f(t - l_1)\, \mathrm{d}l_1 \tag{1.7}$$

$$E\Big\{y(t+\tau)\Big\} = \frac{1}{L_1}\int_{-\frac{L_1}{2}}^{\frac{L_1}{2}} \frac{1}{L_{12}}\int_{-\frac{L_{12}}{2}}^{\frac{L_{12}}{2}} g(t + \tau - l_1 - l_{12})\, \mathrm{d}l_{12}\, \mathrm{d}l_1 \tag{1.8}$$

$$E\Big\{x(t)y(t+\tau)\Big\} = \frac{1}{L_1}\int_{-\frac{L_1}{2}}^{\frac{L_1}{2}} \frac{1}{L_{12}}\int_{-\frac{L_{12}}{2}}^{\frac{L_{12}}{2}} f(t - l_1)\, g(t + \tau - l_1 - l_{12})\, \mathrm{d}l_{12}\, \mathrm{d}l_1 \tag{1.9}$$

Putting (1.7), (1.8) and (1.9) into Eq. (1.2), the final formula for approximate

cross-covariance (AXCF) reads:

$$\widetilde{xcov}(t,\tau) = \frac{1}{L_1 L_{12}} \int_{-\frac{L_1}{2}}^{\frac{L_1}{2}} \int_{-\frac{L_{12}}{2}}^{\frac{L_{12}}{2}} f(t-l_1)\, g(t+\tau-l_1-l_{12})\, \mathrm{d}l_{12}\, \mathrm{d}l_1 -$$

$$-\frac{1}{L_1} \int_{-\frac{L_1}{2}}^{\frac{L_1}{2}} f(t-l_1)\, \mathrm{d}l_1 \;\; \frac{1}{L_1 L_{12}} \int_{-\frac{L_1}{2}}^{\frac{L_1}{2}} \int_{-\frac{L_{12}}{2}}^{\frac{L_{12}}{2}} g(t+\tau-l_1-l_{12})\, \mathrm{d}l_{12}\, \mathrm{d}l_1. \qquad (1.10)$$

Approximate auto-covariance (ACF) can be derived analogously from (1.3), or alternatively from (1.10) considering that the "mother" waveforms are identical $g(t) = f(t)$, and that PDF $p_{12}(l_{12})$ becomes formally a Dirac delta function. The final formula for ACF then reads:

$$\widetilde{cov}(t,\tau) = \frac{1}{L_1} \int_{-\frac{L_1}{2}}^{\frac{L_1}{2}} f(t-l_1)\, f(t+\tau-l_1)\, \mathrm{d}l_1 -$$

$$-\frac{1}{L_1} \int_{-\frac{L_1}{2}}^{\frac{L_1}{2}} f(t-l_1)\, \mathrm{d}l_1 \;\; \frac{1}{L_1} \int_{-\frac{L_1}{2}}^{\frac{L_1}{2}} f(t+\tau-l_1)\, \mathrm{d}l_1. \qquad (1.11)$$

The ACF formula thus requires only specification of the "mother" waveform (i.e. GF in the mean velocity model) and the width of the uniform time shift distribution L_1. Eq. (1.11) is easy to implement as the integrals normalized by $1/L_1$ operate as smoothing by a moving time window of width L_1.

1.3 Stationarized covariance functions

Since the real elastic parameters of the Earth are rather complex (3D, anisotropic, etc.), the covariance determined by ACF and also MC simulations might not reflect the reality perfectly. Nevertheless, we can assume that the overall pattern of the ACFs and simulated CFs effectively captures the main features of the GFs uncertainty. In particular, we consider that such representative of the true uncertainty for each time lag τ is just the CF's average over time, $\frac{1}{T} \int_{-\infty}^{\infty} cov(t,\tau)\, \mathrm{d}t$, where T is duration of the dominant part of the signal. By calculating the mean of the (non-stationary) CF over time we obtain covariance dependent only on the time lag τ, which is property of so-called wide-sense stationary random signals (e.g., Marple 1986), and thus we denote this approach as stationarization. For example, when the stationarized covariance function (SCF) is evaluated from the ACF, we call it stationarized approximate covariance function (SACF),

$$\overline{cov}(\tau) \stackrel{def}{=} \frac{1}{T} \int_{-\infty}^{\infty} \widetilde{cov}(t,\tau)\, \mathrm{d}t. \qquad (1.12)$$

Since the SACFs are by definition stationary (i.e. depending only on lag τ), the respective covariance matrix has Toeplitz structure (see example in Fig. 1.2e).

Such property may be useful in specific (e.g., large-scale or iterative) applications because it permits very cheap calculation of the matrix's inverse, which is required when solving inverse problems (e.g., Tarantola 2005, pp. 62–68).

After substitution of the ACF in Eq. (1.11) into definition of the SACF in Eq. (1.12) the formula for the SACF can be after simple algebra equally expressed as

$$\overline{cov}(\tau) = \frac{1}{T}\left[r_f(\tau) - \wedge_{2L_1}(\tau) * r_f(\tau)\right], \tag{1.13}$$

where $*$ denotes temporal convolution, $\wedge_{2L_1}(\tau)$ is the triangle function of unit area centered around zero with duration $2L_1$, and r_f is auto-correlation $r_f(\tau) \overset{def}{=} \int_{-\infty}^{\infty} f(t)f(t+\tau)\mathrm{d}t$ of the "mother" waveform $f(t)$. The complete derivation of the SACF and the stationarized approximate cross-covariance function (SAXCF) are included in the Thesis.

1.4 Performance in capturing GF variations

Covariance matrices and their approximations are used to statistically describe the uncertainty of the GFs. However, it is not trivial to assess the quality of the proposed approximations in terms of capturing the true variability of the GFs. To address this issue, we draw random GF samples from their multivariate normal distributions described by the "mother" waveforms and the auto-covariance matrices to visually inspect their effects on the GF variability. Examples of random GFs generated considering the various covariance matrices introduced herein are shown in Fig. 1.2.

Random GFs generated using the MC covariance matrix (Fig. 1.2b) may serve as a reference set. They reasonable agree with the variability of the original set of the GFs calculated for the randomly perturbed velocity models (see Fig. 1.1b). Spread of the GFs generated by the ACF matrix (Fig. 1.2d) is very similar to the reference (Fig. 1.2b). Indeed, the random GFs generated using the ACF matrix have similar time shifts as the reference GFs. We note that the variations in GF amplitudes might come as a surprise because the ACF formula in Eq. (1.11) was derived assuming pure time shifts without any change of the signal shape. This is due to the fact that the Gaussian PDF is not mathematically perfect statistical model for capturing such variations. In other words, the variations in amplitudes represent an artifact of using the chosen statistical model for the randomly shifted signal in a mathematical sense. Nevertheless, despite being an artifact, we consider it advantageous for our purpose since the ACF then captures more general variability that is closer to the reference one obtained by the expensive MC approach.

Variability of GFs for the SACF matrix (Fig. 1.2f) is similar to the reference in the time interval where the mother GF has the strongest signal (i.e. $15 - 26\,sec$). Outside of this time interval, the time-independence of the SACF leads to theoretically possible strong amplitude variations unobserved in the reference set. If needed, these variations could be suppressed by applying an additional taper on the rows and columns of the respective covariance matrix.

For illustration purposes we show in Fig. 1.2h also the case of a diagonal covariance matrix since it is most typically considered in current source inversions.

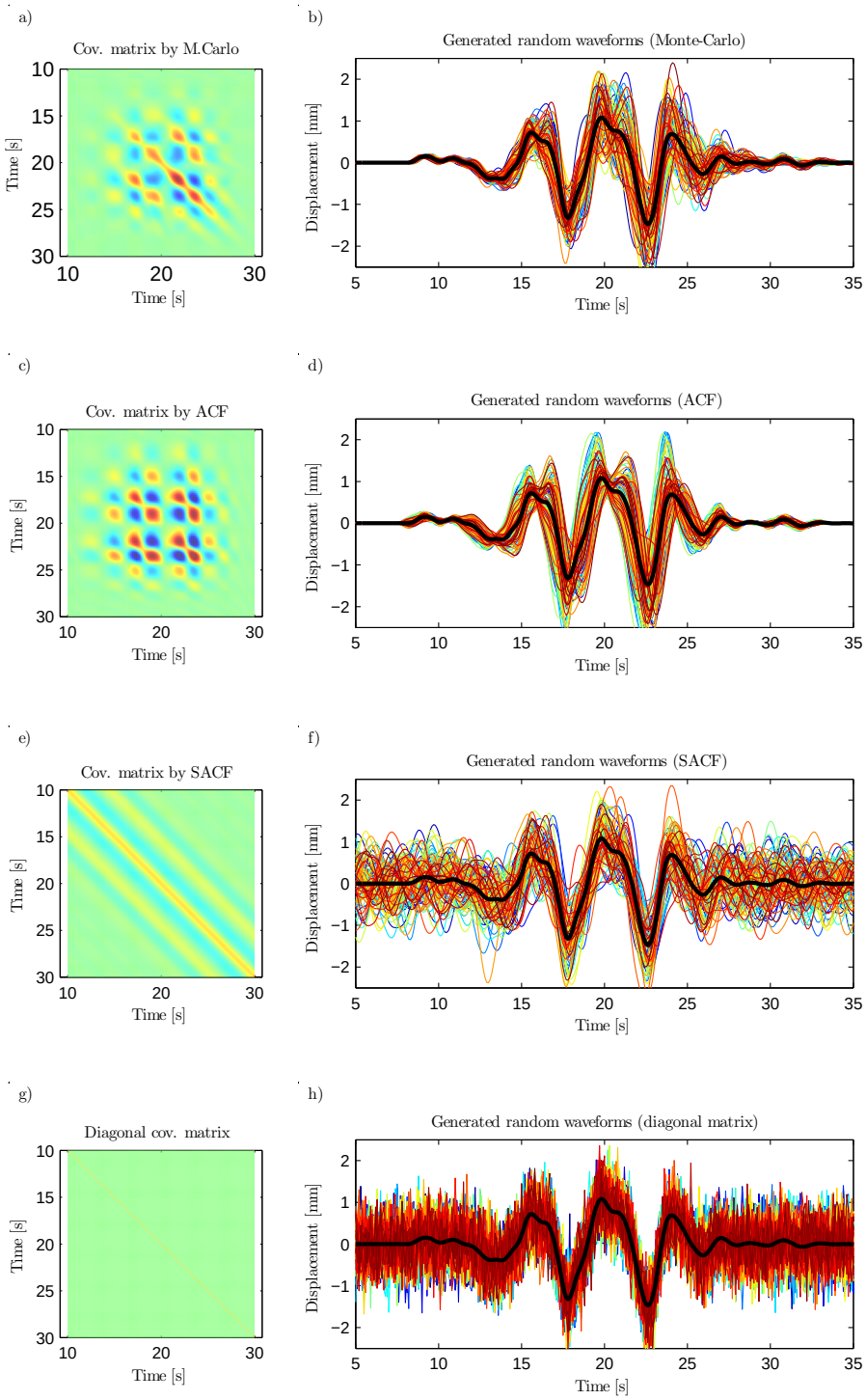

Figure 1.2: *Examples of GFs (**b**, **d**, **f**, **h**) generated as random samples from multivariate Gaussian distributions described by a mother GFs (in bold black) and the various auto-covariance matrices shown in the respective panels (**a**, **c**, **e**, **g**), see legend. Waveform colors have no meaning and are used just for clearer view. The source-receiver distance for this example is* $50\,km$*, and the strength of the model perturbation* $\sigma_M = 10\,\%$.

2. Bayesian source inversion of synthetic data

The proposed approximate covariances can be easily implemented into existing seismic source inversions based on waveform modeling including those formulated in the Bayesian framework. For example, it can be used in source inversion proposed by, e.g., Yagi & Fukahata (2011) or Duputel et al. (2012), where the covariance matrix of the modeling errors (describing the GFs uncertainty) is added to the data covariance matrix describing the seismic noise. In those approaches the covariance of the modeling error is iteratively updated every source model update. Here we show an alternative, simplified, Bayesian approach, assuming that the data error is mainly due to the velocity model uncertainty. In other words, the modeling error covariance is estimated using the approximate formulas in Eqs (1.11) and (1.13) evaluated directly from the observed waveforms. This allows us to solve the inverse problem very efficiently without any iterations.

For the present example of moment tensor (MT) inversion from synthetic data, we consider an earthquake from the Corinth Gulf, Greece, at depth $8\,km$ and with moment magnitude $M_w = 5.4$. Synthetic data were computed by the discrete wavenumber method (Bouchon 1981) assuming a Dirac delta function as the source time function and pure shear mechanism with strike 327°, dip 32°, and rake -45°. In the following tests we generate "data" for the inversion assuming a realization of random variations of the wave speeds and depths of the layers (as in the MC simulations described in previous sections. Such random variations of the reference velocity model simulate a real case when the velocity model is complex, yet well described by a mean velocity model.

2.1 Inversion method

We follow the approach of Kikuchi & Kanamori (1991), where the full seismic MT is parametrized by six elementary MTs defined herein. Full MT is then composed of their linear combination described by six coefficients $(a_1 \dots a_6)$,

$$\mathbf{M} = \sum_{n=1}^{6} a_n \mathbf{M}_n = \begin{pmatrix} a_2 - a_5 + a_6 & a_1 & a_4 \\ a_1 & -a_2 + a_6 & a_3 \\ a_4 & a_3 & a_5 + a_6 \end{pmatrix}. \tag{2.1}$$

For each of the elementary MT n we evaluate elementary seismogram $\boldsymbol{E}_r^n$ by the discrete wavenumber method for a receiver r (vectors $\boldsymbol{E}$ consists of temporal samples). Synthetic seismogram $\boldsymbol{u}_r$ for a general MT in (2.1) can then be obtained by a linear combination of the six elementary seismograms,

$$\boldsymbol{u}_r = \sum_{n=1}^{6} a_n \boldsymbol{E}_r^n = \mathbf{G}\boldsymbol{m} \tag{2.2}$$

where $\boldsymbol{m} = (a_1, a_2, a_3, a_4, a_5, a_6)^T$ and $\mathbf{G}$ is linear operator of the forward problem consisting of the elementary seismograms $\boldsymbol{E}_r^n$. Generalization to more stations and components is straightforward.

The advantage of such linear formulation is the possibility to pre-compute the elementary seismograms for all receivers, and then easily find coefficients including their errors by means of the Bayesian approach (Tarantola 2005, pp. 62–68). Indeed, assuming that observed data $\boldsymbol{d_{obs}}$ are characterized by Gaussian data errors with covariance matrix $\mathbf{C_D}$ and considering no prior information (i.e. infinite standard deviation) on the model parameters $\boldsymbol{m}$, the posterior conditional PDF $p(\boldsymbol{m}|\boldsymbol{d_{obs}})$ reads

$$p(\boldsymbol{m}|\boldsymbol{d_{obs}}) = const.\ \exp\Big(-\frac{1}{2}(\boldsymbol{d_{obs}} - \mathbf{G}\boldsymbol{m})^T\ \mathbf{C_D}^{-1}\ (\boldsymbol{d_{obs}} - \mathbf{G}\boldsymbol{m})\Big) \tag{2.3}$$

where *const.* is a normalization constant. This Gaussian function attains its maximum for

$$\widetilde{\boldsymbol{m}} = \Big(\mathbf{G}^T\ \mathbf{C_D}^{-1}\ \mathbf{G}\Big)^{-1}\ \Big(\mathbf{G}^T\ \mathbf{C_D}^{-1}\ \boldsymbol{d_{obs}}\Big), \tag{2.4}$$

which is called best-fitting or maximum likelihood solution. The shape of the Gaussian PDF is characterized by the (posterior) covariance matrix $\widetilde{\mathbf{C}}^{\mathbf{M}}$ given by

$$\widetilde{\mathbf{C}}^{\mathbf{M}} = \Big(\mathbf{G}^T\ \mathbf{C_D}^{-1}\ \mathbf{G}\Big)^{-1}. \tag{2.5}$$

The 6×6 elements of matrix $\widetilde{\mathbf{C}}^{\mathbf{M}}$ fully describe the uncertainty of the inverted MT solution.

Let us explain an alternative view of the role of the data covariance matrix in the Bayesian inversion. The covariance matrix is by definition positive semidefinite, and if it is, moreover, positive definite, its inverse exists and can be factorized by Cholesky decomposition

$$\mathbf{C_D}^{-1} = \mathbf{R}^T\mathbf{R}, \tag{2.6}$$

where $\mathbf{R}$ is an upper triangular matrix. Putting (2.6) into (2.3), the posterior PDF can be rewritten as

$$p(\boldsymbol{m}|\boldsymbol{d_{obs}}) = const.\ \exp\Big(-\frac{1}{2}(\mathbf{R}\boldsymbol{d_{obs}} - \mathbf{RG}\boldsymbol{m})^T\ (\mathbf{R}\boldsymbol{d_{obs}} - \mathbf{RG}\boldsymbol{m})\Big) \tag{2.7}$$

meaning that the best-fitting solution minimizes L2-norm of so-called standardized residuals obtained as a difference between the data and synthetics after they both are multiplied by the triangular matrix $\mathbf{R}$ from the Cholesky decomposition.

2.2 The maximum likelihood solution

The MT inversion is performed for 1000 different target data sets computed in randomly perturbed velocity models. For each realization, we obtain maximum likelihood solutions in Eq. (2.4) for each type of the covariance matrix considered. Fig. 2.1 shows the ensemble of the solutions displayed in terms of DC mechanism nodal planes, and histograms of maximum difference to the true model in strike, dip, rake, DC component ratio and the inferred scalar seismic moment M_0. We note that the spread of the differences to the reference solution (plotted in red) is caused by variations of the randomly perturbed velocity model, hence by the GFs uncertainty.

The maximum difference in the angles of the DC mechanisms reaches 10–20° depending on the covariance matrix type considered. Asymmetry of the DC

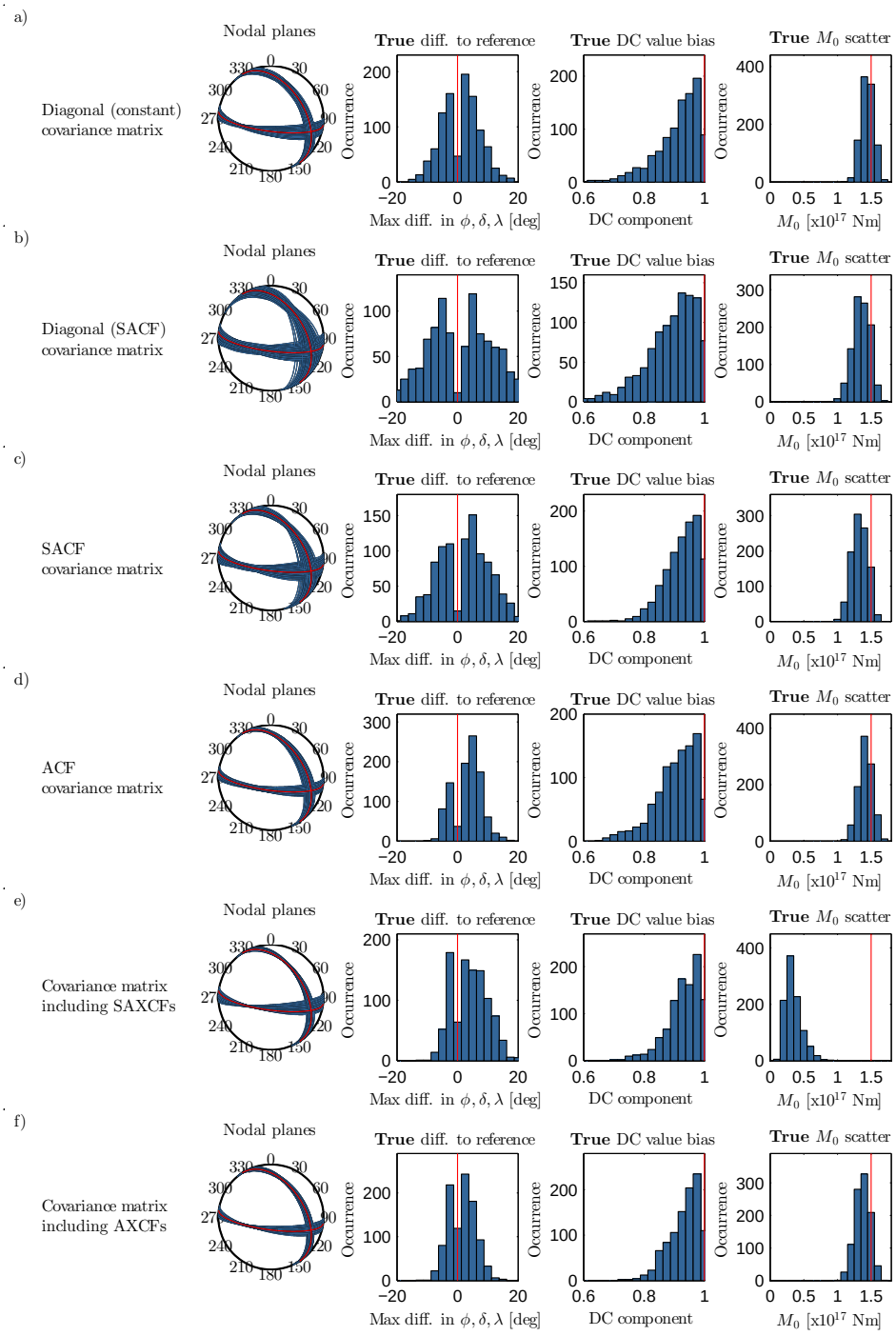

Figure 2.1: *Statistical analysis of maximum likelihood solutions from MT inversion synthetic tests with 1000 realizations of randomly perturbed velocity models used to generate population of target data for the inversion. Panels in each row show DC mechanism nodal planes (left), maximum differences in strike, dip, rake to the reference (middle-left), DC component bias (middle-right) and M_0 scatter (right). Each row corresponds to the use of different type of the data covariance matrix (see legend). The true reference solution (in red) has a pure shear mechanism (DC = 1) with strike 327°, dip 32°, rake -45°, and scalar seismic moment $M_0 = 1.5 \times 10^{17}\, Nm$.*

mechanism angle difference (e.g., Fig. 2.1d) is related to the particular spatial settings of the monitoring network. The DC component ratios are scattered from the simulated pure shear (DC = 1) down to values $0.8 - 0.6$. The variability of the inferred scalar moments is similar for all the considered covariance matrix types ranging from 1.0 to $1.6 \times 10^{17}\, Nm$ (i.e. 5.3 to 5.4 in moment magnitude scale), except for the SAXCF case. Indeed, although nodal planes may be similar to the reference, the scalar seismic moment is underestimated in order to reduce the effect of the temporal averaging of the cross-correlations.

We note that the presented statistics of the inverted maximum likelihood parameters can be understood as the "true" MT uncertainty caused by the velocity model uncertainty. It implies that such MT uncertainty is significant and thus should not be neglected in applications. Therefore, in the next section we assess the ability of the individual types of the covariances to estimate the "true" uncertainty in terms of the posterior covariance matrix.

2.3 Moment tensor uncertainty estimate

We arbitrarily selected one of the synthetic target data sets, inferred the best-fitting MT solution and estimated its uncertainty in terms of the posterior covariance matrix (Eq. (2.5)). For each type of the data covariance matrix, Fig. 2.2 shows the maximum likelihood solution together with the posterior uncertainty similarly to Fig. 2.1. However, here the ensemble of the solutions is obtained by random sampling the posterior PDF (using Matlab function *mvnrnd*). In Fig. 2.2 the true parameters are plotted by red color for comparison. We note that the best-fitting solutions are biased due to the particular velocity model perturbations considered in the target data. In the following we concentrate on the uncertainty estimation in comparison with the "true" uncertainty as revealed in previous Section.

In case of the constant diagonal covariance matrix (Fig. 2.2a) the posterior PDF is characterized by very narrow uncertainty limits in contrast to the "true" uncertainty (Fig. 2.1a). Such estimate of the MT uncertainty is clearly unacceptable. Slightly better, yet still underestimated, uncertainty is attained when including the ACF covariance matrix (Fig. 2.2d in comparison with Fig. 2.1d). However, the uncertainty estimate of ACF covers mostly also the target reference shown by the red line. Inversion with the SACF in Fig. 2.2c provides the largest MT uncertainty estimate, being comparable with that shown in Fig. 2.1c. The larger uncertainty estimate is linked to the time-invariance of the SACF covariance matrix allowing for more general waveform changes as can be seen in Fig. 1.2f. Finally, considering also the inter-component cross-covariances in the inversion reduces the posterior PDF uncertainty estimate for both the SAXCF (Fig. 2.2e) and AXCF (Fig. 2.2f).

To conclude, experiments with the large number of synthetic target datasets obtained by randomly perturbing velocity models reveal that the lowest scatter of the maximum likelihood solutions is attained for the approximate covariance function (ACF and AXCF). Tests also show that the posterior covariance matrix of model parameters reflects the true uncertainty of the MT solution well when considering the stationarized auto-covariance function (SACF)

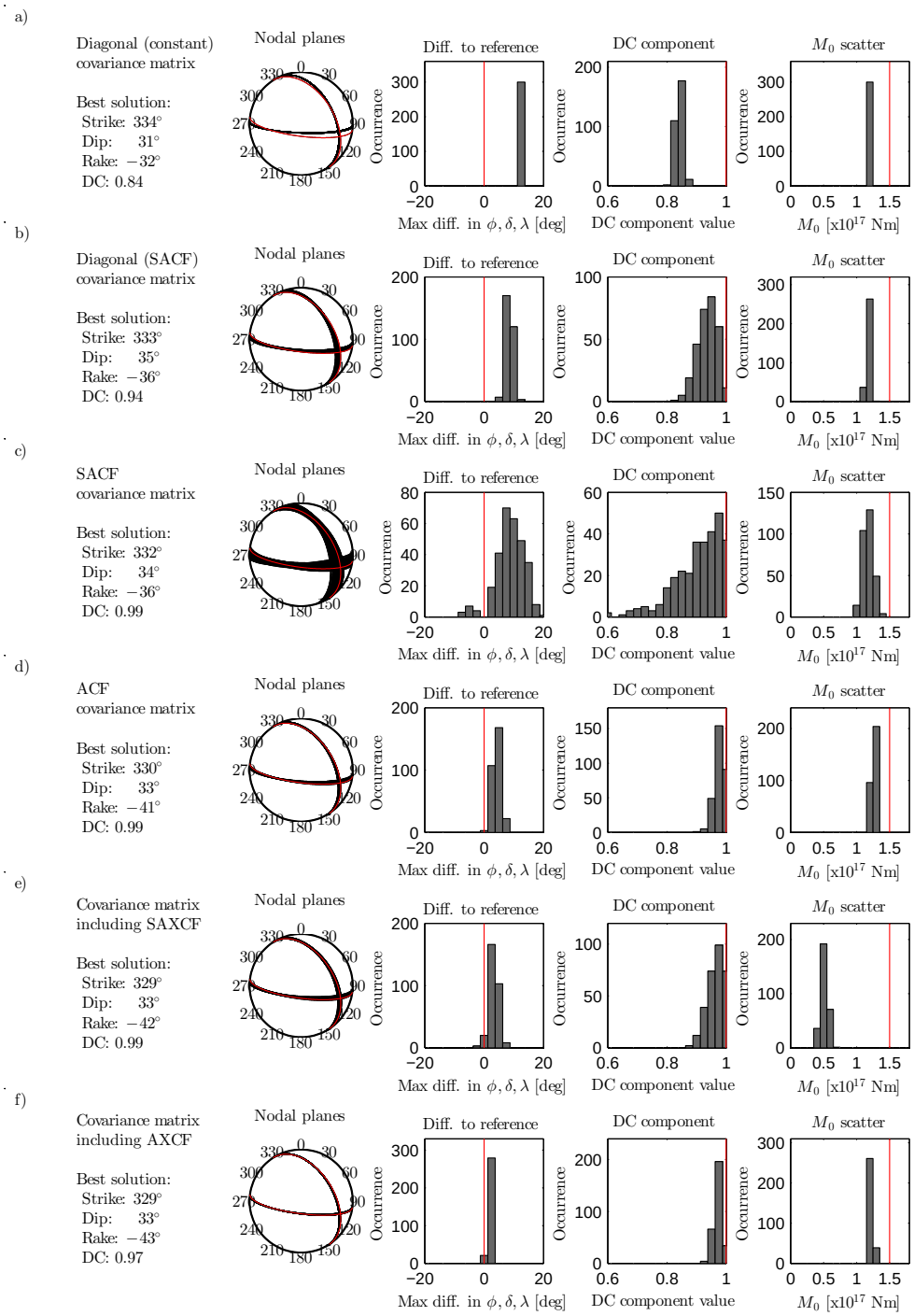

Figure 2.2: *Result of a synthetic MT inversion test with a single realization of the randomly perturbed velocity models to generate the target data. Panels in a row are the maximum likelihood solutions (text), DC mechanism fault planes (left), maximum difference to reference in strike, dip, rake (middle-left), DC component (middle-right) and the M_0 scatter (right). Each row corresponds to the use of different type of the data covariance matrix (see legend). The beach balls and histograms are built from 300 random samples of the posterior PDF to visualize the estimated parameter uncertainty. The true solution (in red) is a pure shear mechanism (DC = 1) with strike 327°, dip 32°, rake -45°, and scalar seismic moment $M_0 = 1.5 \times 10^{17}\, Nm$.*

3. Bayesian source inversion of the 2016 Kumamoto earthquakes

The 2016 Kumamoto earthquake sequence started on April 14, 2016, with an $M_{JMA}6.5$ shallow earthquake in the central part of Kyushu, Japan. The seismic activity continued by weaker events, including $M_{JMA}5.8$ and $M_{JMA}6.4$ earthquakes $41\,min$ and $2.6\,h$ after the first shock, respectively. The mainshock of the sequence of $M_{JMA}7.3$ occurred on April 16, 2016 (01:25 of Japan Standard Time), $28\,h$ after the first earthquake. The mainshock generated destructive ground motions in the near-source region, causing severe damage and casualties. The following aftershocks had wide spatial distribution across the whole Kyushu with the strongest event of $M_{JMA}5.9$ that occurred $20\,min$ after the mainshock.

This earthquake sequence occurred along the Futagawa-Hinagu fault system, which is one of the major active fault zones in Kyushu. This shear zone is considered to be western extension of the Median Tectonic Line, the largest tectonic line in southwestern Japan. The tectonic stress in Kyushu has large spatial heterogeneities. At Kumamoto area, the minimum principal tectonic stress σ_3 is in the N–S direction, and the maximum principal tectonic stress σ_1 has similar size as σ_2; therefore, strike-slip and also normal faults are expected under such stress regime.

3.1 Data and inversion method

We infer centroid moment tensors (CMTs) of 11 significant earthquakes with M_{JMA} magnitude in range of 4.8–6.5. The set consists of all foreshocks and aftershocks with M_{JMA} magnitude higher than or equal to 5, and two aftershocks with M_{JMA} magnitude 4.9 and 4.8. We estimate that more than 99 % of the total scalar seismic moment of the 2016 Kumamoto sequence was released by these events together with the $M_{JMA}7.3$ mainshock.

We use three-component strong-motion waveforms recorded by the K-NET, KiK-net and F-net networks, operated by National Research Institute for Earth Science and Disaster Resilience (NIED), in the distances of $10 - 60\,km$ from the epicenter. The stations are selected based on azimuthal coverage, distance and sufficient signal-to-noise ratio in the low-frequency range. Stations located too close to the epicenter are excluded to comply with the point source approximation.

For the CMTs inversion, we use modification of the Bayesian full-waveform CMT inversion, ISOLA-ObsPy (Vackář et al. 2017), which allows for reliable assessment of the solution uncertainty. As the solution uncertainty is dominated by modeling errors governed by the uncertainty of the GFs due to the inaccuracy of the crustal model considered, we include the modeling errors in covariance matrix $\mathbf{C_D}$ following approach by Hallo & Gallovič (2016). GFs are computed by the discrete wavenumber method (Bouchon 1981) in 1D velocity model consisting of homogenous layers. The model is prepared from the 3D Japan Integrated Velocity Structure Model as a horizontal average over area of $40 \times 40\,km$ around mainshock epicenter.

3.2 Solutions of the CMT inversion

The inferred CMTs of the analyzed events exhibit significant systematic spatial variations throughout the source region (Fig. 3.1). Analyzed CMTs of foreshocks are strike-slip events located near the surface traces of the Hinagu and Futagawa faults (red DC beach-balls in Fig. 3.1). Contrarily, aftershocks have various mechanisms with majority of normal dip-slips (blue DC beach-balls in Fig. 3.1).

Parameters of the inferred solutions together with their uncertainties are compiled in Table 3.1. The percentage of the double-couple (DC) source content spans from 64 to 98 %. In most cases, it is characterized by large uncertainty including also possibility of pure shear (i.e. DC 100 %), and hence, the presence of CLVD component cannot be proved (but also disproved) for most of the inferred CMT solutions. The exceptions are events No. 1, 3 and 7 whose admissible DC values do not exceed 90 % even taking the uncertainty into account. Hence, we consider these events as having a significant CLVD component. Moreover, event No. 7 has the highest variance reduction in all the events, and hence, we consider its significant CLVD component particularly well constrained.

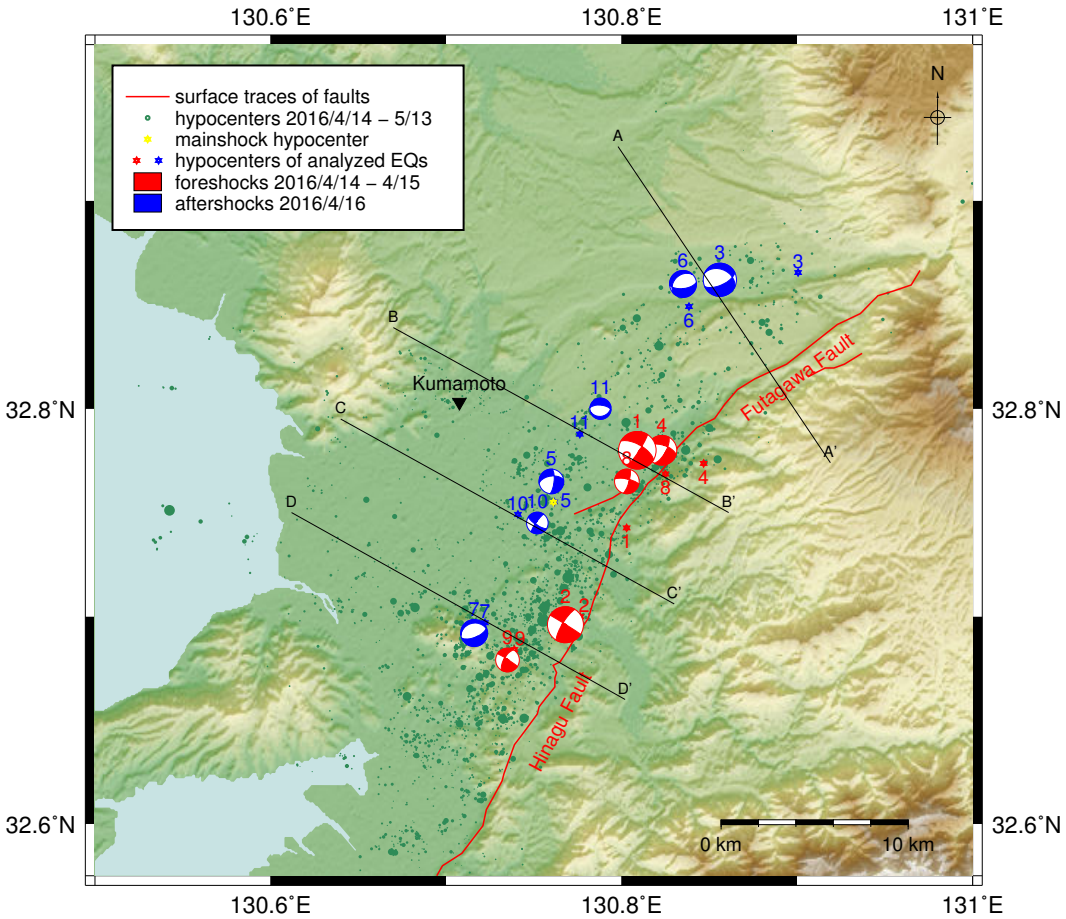

Figure 3.1: *Map of inferred CMTs of the Kumamoto earthquake sequence. CMTs are shown by beach-ball representation of the best DC source. The background seismicity is adopted from Kato et al. (2016). The sizes of the circles are proportional to the JMA magnitude of the events.*

No.	CMT location					DC component		DC component uncertainty	
	Lat.	**Lon.**	**Depth** $[km]$	M_w	**VR** %	**S/D/R** [°]	**DC** %	**S/D/R** [°]	**DC** %
1	32.780	130.809	8.1	6.1	44	33/82/-155	64	3/7/9	±24
2	32.696	130.768	3.8	6.0	58	212/77/178	87	2/9/12	±20
3	32.862	130.856	8.4	5.7	59	294/37/-48	67	6/4/8	±16
4	32.780	130.823	8.3	5.4	73	29/69/-149	94	2/3/4	±10
5	32.765	130.760	13.0	5.0	45	6/72/-142	79	5/7/10	±14
6	32.860	130.835	10.0	5.2	60	83/62/-71	89	3/2/3	±10
7	32.692	130.716	7.8	5.2	74	68/63/-95	75	3/2/3	±8
8	32.765	130.803	9.9	4.9	54	16/76/-163	92	2/4/4	±14
9	32.679	130.735	8.1	4.9	71	211/66/175	90	2/3/3	±8
10	32.745	130.752	5.7	4.7	53	215/81/-165	83	2/7/8	±22
11	32.800	130.788	5.7	4.6	61	79/29/-104	98	8/2/8	±12

Note: VR–variance reduction; M_w–moment magnitude; S/D/R–strike/dip/rake

Table 3.1: *Parameters of the inferred CMT solutions together with their uncertainty in terms of double standard deviation of Gaussian function (2σ) fitted to the respective marginal PDF.*

3.3 Seismo-tectonic interpretation

Foreshocks (red beach-balls in Fig. 3.1) imply right-lateral strike-slip movements in the NE–SW direction in the Hinagu fault zone. Those ruptures located close to the intersection of the Hinagu and Futagawa fault zones are dipping slightly to ESE, while those in the southern area are dipping to WNW. The assumed activated ruptures span from surface to depth of approximately 14 km. Contrarily, aftershocks are mostly normal dip-slip events (blue beach-balls in Fig. 3.1) and spread NW along the assumed fault plane of the $M_{JMA}7.3$ mainshock, where the surface subsidence occurred as documented by InSAR (Himematsu & Furuya 2016). Aftershock's ruptures are situated at depths greater than 5 km, close to the assumed fault plane of the mainshock. These findings imply that foreshocks and partially also mainshock are driven by stresses of the NE–SW shear zone, while aftershocks are mostly related to the N–S extensional stress regime of Beppu–Shimabara graben (Kamata & Kodama 1994).

Co-activation of the right-lateral strike-slips with normal faulting ruptures through the sequence was introduced also by static slip model from geodetic data (Himematsu & Furuya 2016). Field investigation by Toda et al. (2016) shows that surface displacements along the previously mapped active fault traces of the Hinagu–Futagawa fault zone are dominated by right-lateral strike-slip surface displacement up to 2 m. The normal dip-slip aftershocks that occurred along the NW edge of the mainshock rupture had no clear relationship with co-seismic surface ruptures; however, minor surface ruptures in downtown of Kumamoto City have been mapped by InSAR (Himematsu & Furuya 2016). Further surveys on imaging causative source faults beneath the surface are necessary to investigate the relationship between the surface ruptures and the geometry of earthquake source faults.

4. Self-adapting Bayesian inversion of finite-extent sources

The probabilistic kinematic finite-extent source inversions have been introduced by several recent studies. For example, Kubo et al. (2016a) and Minson et al. (2013) take into account the GFs variance, treating the GF variance as an unknown parameter with uniform and log-normal prior PDF, respectively. Duputel et al. (2014, 2015) show the importance of considering the full covariance matrix in inversions, and propose to estimate the full covariance matrices by considering a linear relationship between the GFs and random, generally 3D, perturbations of the velocity model.

Such Bayesian finite-fault inversions estimate the solution uncertainty for the particular choice of parametrization of the source model (e.g., assumptions on spatial smoothing, temporal parametrization, etc.). The choice of parametrization may have a big influence on the inferred solution (e.g., Beresnev 2003), and hence also on the estimated uncertainty of the solution. Therefore, it is advisable to choose the source model parametrization considering the resolution power of the observed data. Over-parametrization is associated with overfitting the observed data (i.e. noise fitting), while under-parametrization is associated with too rough source models.

Our work introduces a non-linear Bayesian fault slip inversion with effective trans-D parametrization of the slip-rate functions (SRFs) and implemented uncertainty of GFs (following Hallo & Gallovič 2016). The performance of our parametric slip inversion method is demonstrated on the inversion of the destructive M_w7.1 mainshock of the 2016 Kumamoto, Japan, earthquake sequence. We infer an ensemble of more than 590k possible finite-source models, representing samples of the posterior probability density function. Such massive ensemble of solutions is then statistically processed to reveal which features of the finite source model of the 2016 Kumamoto mainshock are reliable and which are rather artifacts.

4.1 Rupture parametrization

Assumed activated fault of finite size is considered as a complex tectonic structure composed from several planar fault segments. These fault segments are discretized into subfaults assumed to be small enough to be treated as point sources with respect to the used wavelengths and source-receiver distances. The slip-rate functions' (SRFs) temporal parametrization relies on the regularized Yoffe function (Tinti et al. 2005), which was shown to be compatible with rupture dynamics (e.g., Bizzarri 2012). The rupture times are modeled by a two-dimensional eikonal equation, describing propagation of the rupture-front from a hypocenter along the fault. The hypocenter location, spatially variable rupture-front velocity, rake angles and parameters of SRFs are treated as the unknown source parameters.

All source parameters in the forward computation are interpolated to the subfaults' centers from a sparse net of so-called control points on the fault. We

define two independent systems of spatial control points differing in their spatial positioning and the interpolation method. Firstly, we use a regular grid of control points distributed over the whole fault (see Fig 4.1a). Such system is used for parametrization of spatial distribution of rake, rupture-front velocity, rise time and peak time. The value of any parameter in a subfaults' position is obtained by bilinear interpolation. For spatial distribution of values of slip we will utilize self-adapting parametrization with varying number of movable control points (spline points) where the density of control points can vary spatially (Causse et al. 2017; see Fig 4.1b). In such formulation, positions of spline points are also parameters of the earthquake source model. Such parametrization can effectively adapt to heterogeneities of slip on the activated fault. The varying number of spline points controls the spatial complexity of the resolved slip on the fault, which leads to the self-adapting model space parametrization driven by the observed seismograms.

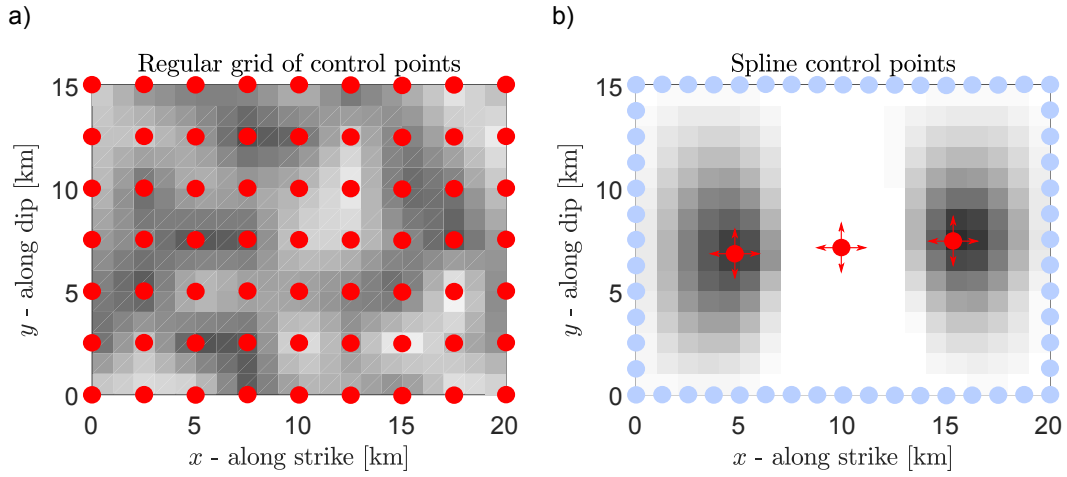

Figure 4.1: *Schemes of two systems of control points used for the spatial parametrization of the rupture. Shaded gray rectangles represent subfaults with parameter values coded by the shade scale. Positions of control points on the fault are shown by red circles for* ***a)*** *regular grid, and* ***b)*** *system of spline points.*

4.2 Exploration of the model space

The forward problem, $\boldsymbol{d} = \boldsymbol{g}(\boldsymbol{m})$, is formulated in the Bayesian probabilistic framework with implemented uncertainty of GFs by Hallo & Gallovič (2016). It is solved as non-linear problem by random exploration of the model space by using the Markov chain Monte Carlo (MCMC) method. Classical MCMC methods sample posterior PDF in particular number of dimensions $\dim(\boldsymbol{m})$, hence, the solution is, in principle, closely related to the selected parametrization. Therefore, we use trans-D MCMC method (Sambridge et al. 2006), where the number of dimensions of the model space (i.e. varying number of spline points) is also subject of inversion, i.e. $\dim(\boldsymbol{m}) \neq const.$

To draw random samples from the multiple-state (i.e. trans-dimensional) posterior PDF $p(\boldsymbol{m}|\boldsymbol{d_{obs}})$, we utilize the reversible jump MCMC algorithm by Green (1995, 2003). The algorithm is based on Metropolis-Hastings algorithm, devel-

oped by Metropolis et al. (1953) and generalized by Hastings (1970), as a Markov chain Monte-Carlo method for sampling posterior PDF by a chain of steps. The used algorithm extends the Metropolis-Hastings to cases when the model change the state between iterates of the Markov chain. The trans-D MCMC is a special case of the reversible jump MCMC algorithm where the proposal moves between model states may be achieved by the "dimension matching". Further, the model states' transitions are considered in one Markov chain step only between neighboring model states. This is so-called birth-death MCMC, and it consists of three move types: "perturb" move with no change in dimensions, "birth" of new dimensions (creation of one arbitrarily spline point), and "death" move, i.e. reducing dimensions (deleting one arbitrarily spline point).

To increase the efficiency of the trans-D MCMC sampler, we apply the Parallel tempering (PT) method introduced by Sambridge (2014). The PT sampling algorithm is similar to the simulated annealing method introducing modification of the posterior PDF by an additional parameter called temperature γ.

To summarize, the utilized trans-D MCMC sampling algorithm with PT in each Markov chain step:

1. Randomly selects the move type (perturb/birth/death).

2. Randomly perturbs the current model to create a new (proposed) model.

3. Creates a new spline point or deletes an existing spline point (only in cases of birth or death moves).

4. Compute forward problem, and then, accepts or rejects the proposed model based on the respective acceptance probability.

5. Tries to exchange the temperature γ with another Markov chain driven by balance condition of Sambridge (2014).

4.3 Application to the mainshock of 2016 Kumamoto sequence

Following Asano & Iwata (2016), we assume a fault plane model consisting of two planar fault segments based on surface traces of known active faults and the aftershock distribution (e.g., Kato et al. 2016). The first fault segment #1 is set along the Hinagu fault intersecting the hypocenter of the M_w7.1 mainshock. The second (larger) fault segment #2 is set along the Futagawa fault spreading to NE from the intersection of both faults (see Fig. 4.2). The Hinagu and Futagawa fault segments are assumed to have rectangular shape of dimension larger than assumed by Asano & Iwata (2016) to not restrain the distance of the rupture propagation.

We use three-component waveforms recorded at 29 stations of the K-NET, KiK-net and F-net strong motion networks operated by NIED, up to the distance of 55 km from the mainshock epicenter (see Fig. 4.2). Few regional stations were excluded, as their waveforms contain complex oscillations probably caused by shallow sedimentary layers. Nevertheless, these stations are located on the edge of the area of interest (see gray triangles in Fiq. 4.2). Original acceleration data

are filtered by a bandpass filter in the range of $0.05 - 0.5\,Hz$ and then integrated into displacements.

GFs are computed by the discrete wavenumber method (Bouchon 1981) in 1D station dependent velocity models consisting of homogenous layers. As the uppermost sedimentary layers may affect the amplitude and shape of the strong motion waveforms at frequencies $0.05 - 0.5\,Hz$, we considered different one-dimensional velocity model for each station. One-dimensional velocity models were extracted from the three-dimensional Japan Integrated Velocity Structure Model as the velocity depth profiles below the receivers.

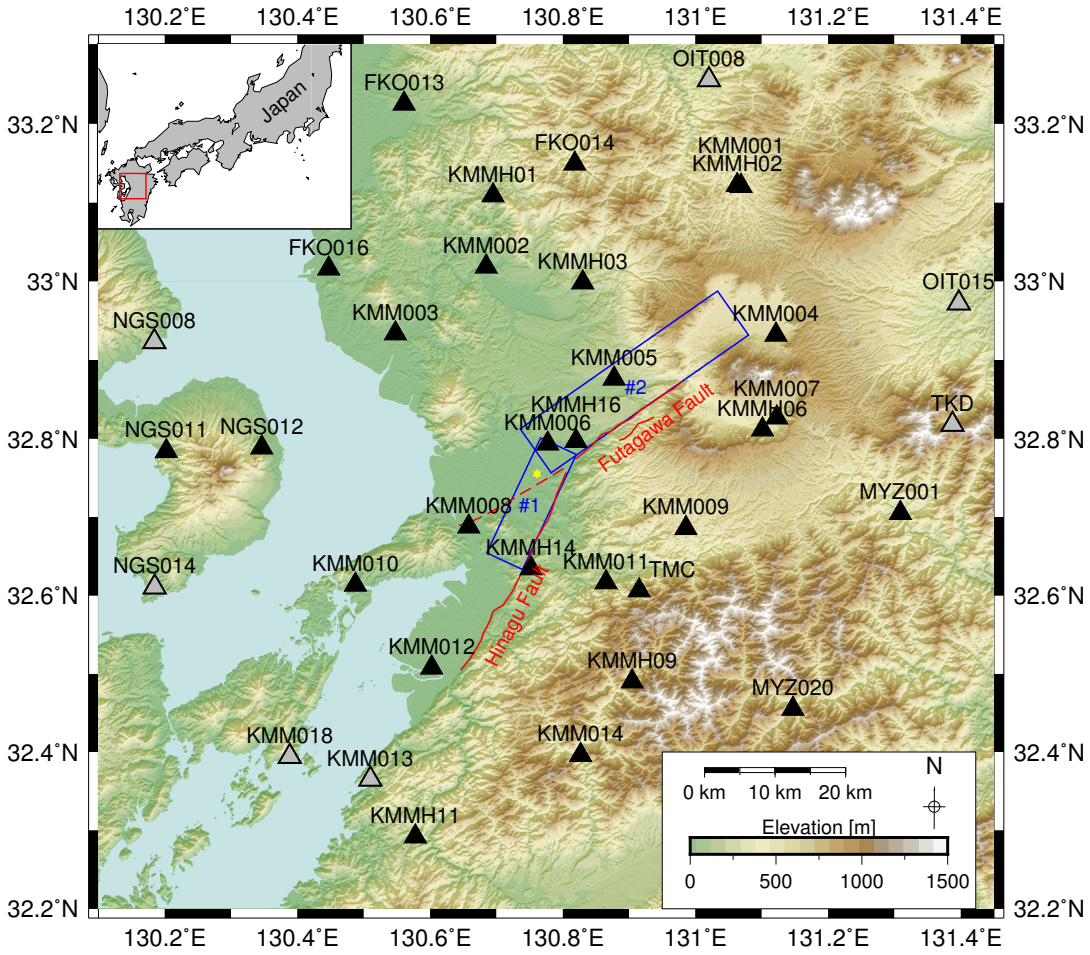

Figure 4.2: *Map of the Kumamoto area, Japan, with the settings of the mainshock inversion (the M_w7.1 earthquake from April 16, 2016). Blue rectangles denote projection of the assumed Hinagu (#1) and Futagawa (#2) fault segments, and the yellow star is the epicenter of the mainshock (from the JMA earthquake catalog). Black triangles show positions of strong motion stations of the K-NET, KiK-net and F-net networks used in the inversion. The gray triangles are stations excluded from the inversion (see text). Red lines denote surface traces of the main known active faults.*

The maximum likelihood solution estimate for the mainshock fault slip inversion is shown in Fig. 4.3. The slip values with denoted rake angles (slip direction) are illustrated for all the subfaults in Figs 4.3a and 4.3b. In Figs 4.3c and 4.3d we show rupture times on the both the fault segments. The inferred source model

has seismic moment of $6.74 \times 10^{19}\, Nm$ ($M_w = 7.2$). The maximum and average slip values are 6.29 and 1.29 m, respectively. The variance reduction is 78.5 %, which indicates good fit of observed and synthetic standardized waveforms.

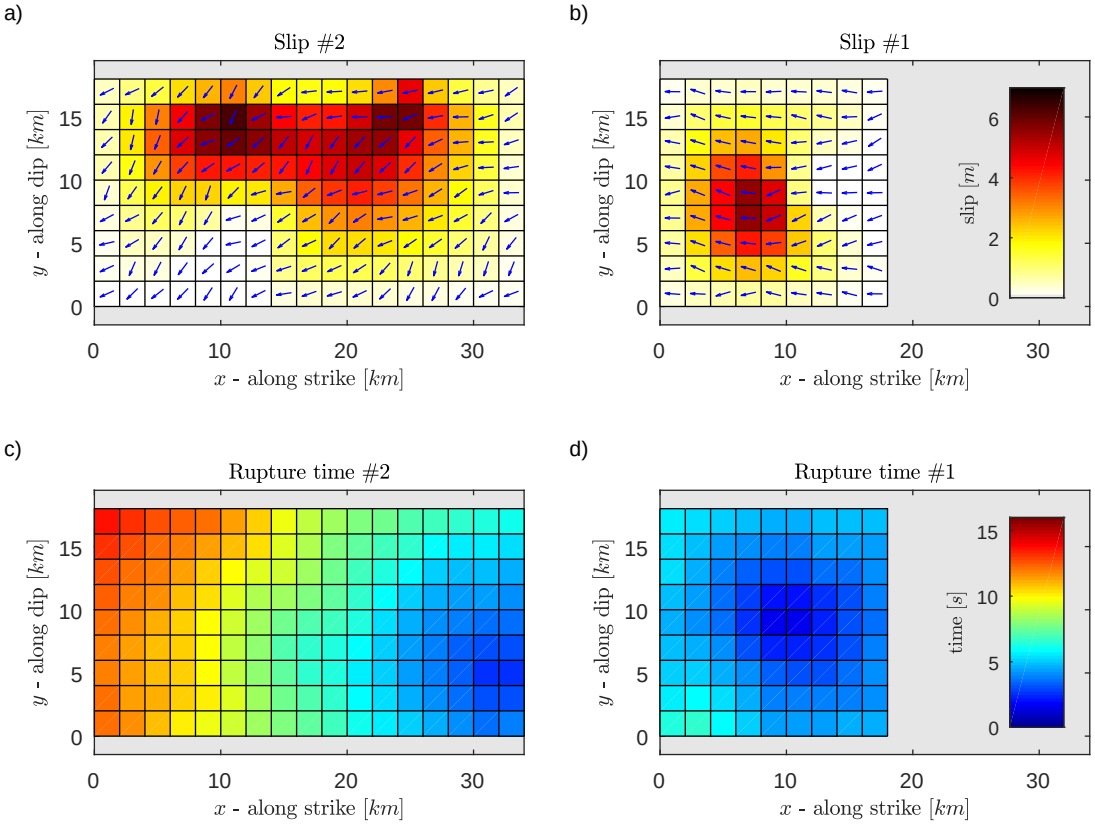

Figure 4.3: *Slip* ***a***, ***b)*** *and rupture times* ***c***, ***d)*** *of the maximum likelihood solution of the M_{JMA}7.3 mainshock inversion on the* ***a***, ***c)*** *Futagawa (#2) and* ***b***, ***d)*** *Hinagu (#1) fault segments. The squares represent 2×2 km subfaults spatially distributed along strike x and along dip y directions, where $(0, 0)$ is the bottom-left corner of the fault footwall. The final slip values and the rupture times are shown by color (see colorbars). The rake angles (slip directions) are shown by blue arrows.*

The maximum likelihood solution estimate has hypocenter located at the Hinagu segment (#1) at the depth of 9 km. The rupture propagates by the average rupture velocity of 2.5 km/s along segment #1, terminating at the intersection of the both fault segments. A large slip on fault segment #1 is concentrated in the zone between the hypocenter and intersection with the fault segment #2 at the depth of approximately $6 - 14\, km$. The inferred origin time in the Futagawa segment (#2) is delayed by 1.2 sec after the origin in segment #1. The hypocenter on segment #2 is located approximately at depth of 13 km at the intersection of the fault segments. The rupture then continuous upward and to NE along segment #2 by the average rupture velocity of 2.7 km/s (see Fig. 4.3c). The largest slip on fault segment #2 is concentrated at shallower parts at depths of approximately $1 - 8\, km$. The rupture terminates at the shallow depths inside the Aso volcano caldera. The inferred rake angles in the segment #1 are close to

pure right-lateral strike-slip movement. Contrarily, the slip directions on segment #2 have significant normal-slip component.

The maximum likelihood solution estimate is not a unique solution, it is rather one of many possible source models that fit the data well. The ensemble of the total of 590 264 possible finite fault source models (with variance reduction in range of $74 - 78.5\,\%$) allows statistical evaluation of the inferred source parameters and an assessment of the model uncertainty. To show statistics of the slip distribution we introduce in the Thesis a modified polar histogram plot called slip disc histogram (SDH). It shows the occurrence of the slip values on individual subfaults as captured by the ensemble of all the finite model solutions. The SDH plot for the ensemble of solutions of the $M_{JMA}7.3$ mainshock inversion shows that the slip on fault segment #1 exhibits high uncertainty, especially in the deepest part. The maximum slip in this segment is in the range of $2.6 - 5.7\,m$. On the other hand, the low slip value in the southernmost part of segment #1 is a feature supported by the whole ensemble. The SDH plot for segment #2 suggests that the maximum slip is in the range of $4.2 - 7.5\,m$. The slip value is well resolved in the southwestern part, while it has large uncertainty in the shallow northeastern zone, i.e. in the Aso volcano caldera.

Conclusion

This Thesis is focused on the influence of crustal velocity model uncertainty on inferred earthquake source parameters. In particular, in Thesis Chapter 2 (also published as Hallo & Gallovič 2016), we perform Monte-Carlo simulations of GFs in randomly perturbed velocity models to reveal the effects of the imprecise velocity model on the synthetic waveforms. Based on the learned knowledge, we derive closed-form formulas for approximate covariance functions to obtain fast and effective characterization of the GFs' uncertainty. These approximate covariance functions require a GF calculated using a given (mean) velocity model and statistical description of the assumed random time shifts of the signal as an input. Experiments indicate that it is enough to assume a uniform PDF for the time shifts of GFs. The width of the uniform PDF denoted as L_1 depends on the source distance and velocity model perturbations linearly, and can be implemented by a simple formula. Further, we point out that despite the fact that the simplified formulas were derived assuming purely random time shifts of GFs, the proposed approach produces variations of both the arrival time and the waveform amplitudes as shown in Fig. 1.2.

The proposed approximate covariance functions are tested on Bayesian moment tensor inversions of synthetic and real data sets. Experiments with the large number of synthetic target datasets obtained by randomly perturbing velocity models reveal that the lowest scatter of the maximum likelihood solutions is attained for the approximate covariance function (ACF and AXCF). Tests also show that the posterior covariance matrix of model parameters reflects the true uncertainty of the MT solution well when considering the stationarized autocovariance function (SACF). Similarly, real-data inversion using the SACF pro-

vides MT uncertainty estimate comparable to the result of the jack-knifing experiment. Finally, additional synthetic tests imply that using SACF in Bayesian inversion allows reliable assessment of the CLVD component uncertainty. For easier implementation in other researchers' codes we release open source codes for computing all the types of the proposed ACFs and SACFs. The source codes in "Fortran90" and "Matlab" programming languages are available under GNU license on the author's website (`http://geo.mff.cuni.cz/~hallo/`) or in Thesis Attachments.

We have extended the Bayesian full-waveform CMT inversion code package ISOLA-ObsPy (Vackář et al. 2017) with the source code for assessment of GFs' uncertainties by ACFs and SACFs. The modified ISOLA-ObsPy is successfully applied on selected earthquakes from the Kumamoto, Kyushu, Japan, earthquake sequence of April 2016 with M_{JMA} magnitude in range of 4.8–6.5. The use of SACF covariance matrices in the Bayesian inversion allow us to perform realistic assessment of the uncertainties of the CMTs (Table 3.1. The inferred CMT solutions show systematic spatial and temporal variations (Fig. 3.1). We estimate geometry of the major activated ruptures and interpret them in the seismotectonic framework. Foreshocks imply right-lateral NE–SW strike-slip movements in the Hinagu fault zone. Aftershocks are mostly normal dip-slip events spreading along the NW edge of the assumed mainshock fault plane. The inferred CMTs with significant CLVD component may suggest a complex source processes, however this issue is still open because of non-uniqueness of the non-DC MTs' decomposition. Therefore, the realistic assessment of the uncertainties of the inferred CMTs proved to be useful in terms of interpretation.

In last Chapter of Thesis we develop a new Bayesian non-linear fault slip inversion which accounts for the GFs' uncertainty by means of the approximate covariance functions (ACF and SACF). The utilized self-adapting parametrization of slip function (by varying number of unattached spline control points) captures features of the slip functions discernible by the observed waveforms.

The Bayesian fault slip inversion is applied on the destructive $M_{JMA}7.3$ mainshock of the 2016 Kumamoto, Japan, earthquake sequence of April 16th, 2016 (01:25 of JST). According to our solution the mainshock started on the Hinagu fault segment as right-lateral pure strike-slip movement. The rupture propagated along the Hinagu fault reaching the intersection of the Hinagu and Futagawa fault segments. Then, the rupture extended upward and to NE along the Futagawa fault segment as a strike-slip with a normal faulting component. The largest slip of $4.2 - 7.5\,m$ took place on the Futagawa fault segment. Statistics from the ensemble of possible solutions then show that the above features are well constrained, being also consistent with other researchers' models (e.g., Asano & Iwata 2016; Kubo et al. 2016b; Yoshida et al. 2017; Himematsu & Furuya 2016). Contrarily, the uncertainty analysis reveals that the zone of the largest slip on the Hinagu fault segment and the slip at the shallow depth inside the Aso caldera are less constrained. The latter is in agreement with the fact that these features are not consistently imaged in the other published source models. The inferred source model of the mainshock supplemented by its uncertainty completes the analysis of the evolution of the Kumamoto sequence in the seismotectonic framework.

Bibliography

Asano, K. & Iwata, T., 2016. Source rupture processes of the foreshock and mainshock in the 2016 Kumamoto earthquake sequence estimated from the kinematic waveform inversion of strong data, *Earth, Planets and Space*, **68:147**, 1–11.

Beresnev, I. A., 2003. Uncertainties in finite-fault slip inversions: To what extent to believe? (A critical review), *Bulletin of the Seismological Society of America*, **93**(6), 2445–2458.

Bizzarri, A., 2012. Analytical representation of the fault slip velocity from spontaneous dynamic earthquake models, *Journal of Geophysical Research*, **117**, B06309.

Bouchon, M., 1981. A simple method to calculate Green's functions for elastic layered media, *Bulletin of the Seismological Society of America*, **71**, 959–971.

Causse, M., Cultrera, G., Moreau, L., Herrero, A., Schiappapietra, E., & Courboulex, F., 2017. Bayesian rupture imaging in a complex medium: The 29 May 2012 Emilia, Northern Italy, earthquake, *Geophysical Research Letters*, **44**(15), 7783–7792.

Dettmer, J., Dosso, S. E., & Holland, C. W., 2007. Uncertainty estimation in seismo-acoustic reflection travel-time inversion, *The Journal of the Acoustical Society of America*, **122**, 161–176.

Dettmer, J., Benavente, R., Cummins, P. R., & Sambridge, M., 2014. Transdimensional finite-fault inversion, *Geophysical Journal International*, **199**, 735–751.

Duputel, Z., Rivera, L., Fukahata, Y., & Kanamori, H., 2012. Uncertainty estimations for seismic source inversions, *Geophysical Journal International*, **190**(2), 1243–1256.

Duputel, Z., Agram, P. S., Simons, M., Minson, S. E., & Beck, J. L., 2014. Accounting for prediction uncertainty when inferring subsurface fault slip, *Geophysical Journal International*, **197**(1), 464–482.

Duputel, Z., Jiang, J., Jolivet, R., Simons, M., Rivera, L., Ampuero, J.-P., Riel, B., Owen, S. E., Moore, A. W., Samsonov, S. V., Ortega Culaciati, F., & Minson, S. E., 2015. The Iquique earthquake sequence of April 2014: Bayesian modeling accounting for prediction uncertainty, *Geophysical Research Letters*, **42**(19), 7949–7957.

Gallovič, F. & Zahradník, J., 2012. Complexity of the M_w 6.3 2009 L'Aquila (central Italy) earthquake: 1. Multiple finite-extent source inversion, *Journal of Geophysical Research*, **117**, B04307.

Gallovič, F., Imperatori, W., & Mai, P. M., 2015. Effects of three-dimensional crustal structure and smoothing constraint on earthquake slip inversions: case study of the M_w 6.3 2009 L'Aquila earthquake, *Journal of Geophysical Research*, **120**, 428–449.

Green, P. J., 1995. Reversible jump Markov chain Monte Carlo computation and Bayesian model determination, *Biometrika*, **82**(4), 711–732.

Green, P. J., 2003. *Trans-dimensional Markov chain Monte Carlo, In: Highly Structured Stochastic Systems*, Oxford University Press, Oxford Statistical Science Series edn.

Hallo, M. & Gallovič, F., 2016. Fast and cheap approximation of Green functions uncertainty for waveform-based earthquake source inversions, *Geophysical Journal International*, **207**(2), 1012–1029.

Hallo, M., Asano, K., & Gallovič, F., 2017. Bayesian inference and interpretation of centroid moment tensors of the 2016 Kumamoto earthquake sequence, Kyushu, Japan, *Earth, Planets and Space*, **69:134**, 1–19.

Hastings, W. K., 1970. Monte Carlo sampling methods using Markov Chains and their applications, *Biometrika*, **57**, 97–109.

Himematsu, Y. & Furuya, M., 2016. Fault source model for the 2016 Kumamoto earthquake sequence based on ALOS-2/PALSAR-2 pixel-offset data: evidence for dynamic slip partitioning, *Earth, Planets and Space*, **68:169**, 1–10.

Kamata, H. & Kodama, K., 1994. Tectonics of an arc-arc junction: an example from Kyushu Island at the junction of the Southwest Japan Arc and the Ryukyu Arc, *Tectonophysics*, **233**(1-2), 69–81.

Kanamori, H. & Rivera, L., 2006. *Energy partitioning during an earthquake, In: Radiated Energy and the Physics of Faulting*, American Geophysical Union, geophysical monograph series edn.

Kato, A., Fukuda, J., Nakagawa, S., & Kazushige, O., 2016. Foreshock migration preceding the 2016 M_w 7.0 Kumamoto earthquake, *Jpn Geophysical Research Letters*, **43**(17), 8945–8953.

Kikuchi, M. & Kanamori, H., 1991. Inversion of complex body waves—III, *Bulletin of the Seismological Society of America*, **81**(6), 2335–2350.

Kubo, H., Asano, K., Iwata, T., & Aoi, S., 2016a. Development of fully Bayesian multiple-time-window source inversion, *Geophysical Journal International*, **204**(3), 1601–1619.

Kubo, H., Suzuki, W., Aoi, S., & Sekiguchi, H., 2016b. Source rupture processes of the 2016 Kumamoto, Japan, earthquakes estimated from strong-motion waveforms, *Earth, Planets and Space*, **68:161**, 1–13.

Marple, S. L., 1986. *Digital Spectral Analysis: With Applications*, Prentice-Hall, Inc., Upper Saddle River, NJ, USA.

Metropolis, N., Rosenbluth, A., Rosenbluth, M., Teller, A., & Teller, E., 1953. Equation of state calculations by fast computing machines, *The Journal of Chemical Physics*, **21**, 1081–1092.

Minson, S. E., Simons, M., & Beck, J. L., 2013. Bayesian inversion for finite fault earthquake source models. I—Theory and algorithm, *Geophysical Journal International*, **194**(3), 1701–1726.

Minson, S. E., Simons, M., Beck, J. L., Ortega, F., Jiang, J., Owen, S. E., Moore, A. W., Inbal, A., & Sladen, A., 2014. Bayesian inversion for finite fault earthquake source models – II: the 2011 great Tohoku-oki, Japan earthquake, *Geophysical Journal International*, **198**, 922–940.

Mustać, M. & Tkalčić, H., 2016. Point source moment tensor inversion through a Bayesian hierarchical model, *Geophysical Journal International*, **204**(1), 311–323.

Piatanesi, A., Cirella, A., Spudich, P., & Cocco, M., 2007. A global search inversion for earthquake kinematic rupture history: application to the 2000 western Tottori, Japan earthquake, *Journal of Geophysical Research*, **112**, B07314.

Sambridge, M., 2014. A Parallel Tempering algorithm for probabilistic sampling and multimodal optimization, *Geophysical Journal International*, **196**(1), 357–374.

Sambridge, M., Gallagher, K., Jackson, A., & Rickwood, P., 2006. Transdimensional inverse problems, model comparison and the evidence, *Geophysical Journal International*, **167**, 528–542.

Sokos, E., Kiratzi, A., Gallovič, F., Zahradník, J., Serpetsidaki, A., Plicka, V., Janský, J., Kostelecký, J., & Tselentis, G.-A., 2015. Rupture process of the 2014 Cephalonia, Greece, earthquake doublet (M_w 6) as inferred from regional and local seismic data, *Tectonophysics*, **656**, 131–141.

Tarantola, A., 2005. *Inverse Problem Theory and Methods for Model Parameter Estimation*, Society for Industrial and Applied Mathematics, Philadelphia.

Tarantola, A. & Valette, B., 1982. Inverse problems = quest for information, *Journal of Geophysics*, **50**(3), 159–170.

Tinti, E., Fukuyama, E., Piatanesi, A., & Cocco, M., 2005. A kinematic source-time function compatible with earthquake dynamics, *Bulletin of the Seismological Society of America*, **95**(4), 1211–1223.

Toda, S., Kaneda, H., Okada, S., Ishimura, D., & Mildon, Z. K., 2016. Slip-partitioned surface ruptures for the M_w 7.0 16 April 2016 Kumamoto, Japan, earthquake, *Earth, Planets and Space*, **68:188**, 1–11.

Vackář, J., Gallovič, F., Burjánek, J., Zahradník, J., & Clinton, J., 2017. Bayesian ISOLA: new tool for automated centroid moment tensor inversion, *Geophysical Journal International*, **210**(2), 693–705.

Valentine, A. P. & Trampert, J., 2012. Assessing the uncertainties on seismic source parameters: towards realistic error estimates for centroid-moment-tensor determinations, *Physics of the Earth and Planetary Interiors*, **210–211**, 36–49.

Yagi, Y. & Fukahata, Y., 2011. Introduction of uncertainty of Green's function into waveform inversion for seismic source processes, *Geophysical Journal International*, **186**(2), 711–720.

Yoshida, K., Miyakoshi, K., Somei, K., & Irikura, K., 2017. Source process of the 2016 Kumamoto earthquake (M_j7.3) inferred from kinematic inversion of strong-motion records, *Earth, Planets and Space*, **69:64**, 1–13.

Zahradník, J. & Custódio, S., 2012. Moment tensor resolvability: application to Southwest Iberia, *Bulletin of the Seismological Society of America*, **102**(3), 1235–1254.

Zahradník, J., Fojtíková, L., Carvalho, J., Barros, L. V., Sokos, E., & Janský, J., 2015. Compromising polarity and waveform constraints in focal-mechanism solutions; the Mara Rosa 2010 M_w 4 central Brazil earthquake revisited, *Journal of South American Earth Sciences*, **63**, 323–333.

List of included publications and citation report

Hallo, M., Asano, K. & Gallovič, F., 2017. Bayesian inference and interpretation of centroid moment tensors of the 2016 Kumamoto earthquake sequence, Kyushu, Japan, *Earth, Planets and Space*, **69**:134, 1–19.

- 1 impact journal citation (without self-citations)

Hallo, M. & Gallovič, F., 2016. Fast and cheap approximation of Green functions uncertainty for waveform-based earthquake source inversions, *Geophysical Journal International*, **207**(2), 1012–1029.

- 12 impact journal citations (without self-citations)